

## The Seasonal Cycle of Gravity Wave Drag in the Middle Atmosphere

MANUEL PULIDO

*Physics Department, FACENA, Universidad Nacional del Nordeste, and CONICET, Corrientes, Argentina*

JOHN THUBURN

*Mathematics Research Institute, School of Engineering, Computing and Mathematics, University of Exeter, Exeter, United Kingdom*

(Manuscript received 20 April 2007, in final form 5 February 2008)

### ABSTRACT

Using a variational technique, middle atmosphere gravity wave drag (GWD) is estimated from Met Office middle atmosphere analyses for the year 2002. The technique employs an adjoint model of a middle atmosphere dynamical model to minimize a cost function that measures the differences between the model state and observations. The control variables are solely the horizontal components of GWD; therefore, the minimization determines the optimal estimate of the drag. For each month, Met Office analyses are taken as the initial condition for the first day of the month, and also as observations for each successive day. In this way a three-dimensional GWD field is obtained for the entire year with a temporal resolution of 1 day. GWD shows a pronounced seasonal cycle. During solstices, there are deceleration regions of the polar jet centered at about 63° latitude in the winter hemisphere, with a peak of 49 m s<sup>-1</sup> day<sup>-1</sup> at 0.24 hPa in the Southern Hemisphere; the summer hemisphere also shows a deceleration region but much weaker, with a peak of 24 m s<sup>-1</sup> day<sup>-1</sup> centered at 45° latitude and 0.6 hPa. During equinoxes GWD is weak and exhibits a smooth transition between the winter and summer situation. The height and latitude of the deceleration center in both winter and summer hemispheres appear to be constant. Important longitudinal dependencies in GWD are found that are related to planetary wave activity; GWD intensifies in the exit region of jet streaks. In the lower tropical stratosphere, the estimated GWD shows a westward GWD descending together with the westward phase of the quasi-biennial oscillation. Above, GWD exhibits a semiannual pattern that is approximately out of phase with the semiannual oscillation in the zonal wind. Furthermore, a descending GWD pattern is found at those heights, similar in magnitude and sign to that in the lower stratosphere.

### 1. Introduction

Using large-scale temperature measurements to determine radiative heating rates, Murgatroyd and Singleton (1961) calculated meridional and vertical winds from the zonal-mean thermodynamic equation and the zonal-mean mass conservation equation. They showed that the global-scale mesospheric mean circulation is basically a cell with ascending air in the summer hemisphere at 40–70 km and subsident motion in the winter hemisphere at 50–80 km, which are connected by a meridional circulation from the summer to the winter

hemisphere. This circulation explains the high temperatures observed in the winter mesosphere.

Lindzen (1981) realized that an isotropic gravity wave spectrum generated at tropospheric levels would be filtered in a systematic way by the background wind in the middle atmosphere leading to a systematic forcing by gravity waves in the upper stratosphere and lower mesosphere. The seasonal variation of gravity wave drag (GWD) produced by gravity wave filtering deduced by Lindzen (1981) is in agreement with the missing force necessary to drive the Murgatroyd and Singleton circulation, that is, the force that balances the Coriolis force produced by the meridional circulation. This evidence suggests that GWD is the main factor responsible for producing the Murgatroyd and Singleton circulation. Thus, Murgatroyd and Singleton's original technique may be used to diagnose GWD in the

---

*Corresponding author address:* Manuel Pulido, Facultad de Ciencias Exactas, UNNE, Av. Libertad 5400, Corrientes 3400, Argentina.  
E-mail: pulido@unne.edu.ar

middle atmosphere if large-scale wave effects are negligible.

Hamilton (1983) estimated the meridional circulation taking into account heat fluxes produced by large-scale waves. Then the imbalance between the Coriolis force and the large-scale momentum flux divergences in the zonal-mean momentum equation can be assigned entirely to small-scale waves. The technique was used to diagnose the zonal-mean monthly averaged GWD in the Northern Hemisphere. A deceleration center is found in December–January located at  $50^{\circ}$ – $60^{\circ}$ , depending on the year. Peak values are  $-15 \text{ m s}^{-1} \text{ day}^{-1}$  at 0.4 hPa.

Shine (1989) employed a similar zonal-mean budget technique to diagnose the seasonal cycle of GWD in both hemispheres from the transformed Eulerian mean equations. He found important interhemispheric differences in winter. In the Southern Hemisphere GWD decelerates the mean flow at a maximum rate of  $-50 \text{ m s}^{-1} \text{ day}^{-1}$  at 0.1 hPa, while in the Northern Hemisphere peak deceleration is about  $-30 \text{ m s}^{-1} \text{ day}^{-1}$  at 0.2 hPa. Marks (1989) further extended the technique assuming a steady flow without zonal averaging, solving iteratively the resulting steady-flow primitive equations with a residual term in the zonal momentum equation. In this way, the three-dimensional structure of GWD is obtained. Again a winter deceleration center is found. Peak values are also stronger in the Southern Hemisphere, reaching  $-55 \text{ m s}^{-1} \text{ day}^{-1}$  at about 0.1 hPa during the whole winter June–August. In the Northern Hemisphere peak values are  $-35 \text{ m s}^{-1} \text{ day}^{-1}$  at  $\sim 0.3$  hPa in November–December. Regrettably, longitudinal behavior of GWD was not shown in Marks's work.

Using a zonal-mean budget technique, Alexander and Rosenlof (2003) determined GWD in the equatorial region. The estimated GWD is consistent with the forces expected to drive the quasi-biennial oscillation (QBO) and semiannual oscillation (SAO). The descent of the eastward phase of the QBO is associated with eastward GWD, while the descent of the westward phase is associated with westward GWD. At higher altitudes where the SAO is located, GWD is found to be out of phase with zonal winds.

In this work we examine the seasonal cycle of GWD throughout the middle atmosphere from 100 to 0.24 hPa using a technique based on variational data assimilation. Met Office analysis data (Swinbank and O'Neill 1994) for the year 2002 are used as observations. During this year the Met Office assimilation system does not change, and the imposed forcing to mimic GWD in the dynamical model is a simple Rayleigh friction term instead of a gravity wave parameterization so that dur-

ing this year we can evaluate readily whether GWD estimations are resulting from observations or from the prescribed forcing. The optimal GWD is estimated by minimizing the differences between a hydrostatic primitive equation middle atmosphere model and observations. The technique, called assimilation system for drag estimation (ASDE), has been tested in twin experiments (Pulido and Thuburn 2005) and in a one-week case study using Met Office data (Pulido and Thuburn 2006). The technique uses the full three-dimensional time evolving governing equations; it does not depend on taking zonal means or on an assumption of steady flow. In this way, it allows the day-to-day variability of GWD and its three-dimensional distribution including longitudinal dependencies to be estimated.

The estimated GWD may be useful to constrain some of the many free parameters that are tuned subjectively in present gravity wave parameterizations (Hines 1997; Warner and McIntyre 1996). However, it is important to note that ASDE estimates the GWD, that is, the divergence of gravity wave pseudomomentum flux. Thus, we obtain only indirect information on gravity wave sources and pseudomomentum fluxes.

The identification of the bias between a dynamical model and analyses as GWD is based on the assumption that other model errors make a negligible contribution to that bias. However, approximations in the radiation scheme, a low-resolution grid, approximations in the numerical representation of the equations, etc., may also be identified erroneously as GWD by ASDE. Nevertheless, we expect GWD to be the dominant effect (Hamilton 1983). Another point of contention is that errors in the analyses (e.g., Bowman et al. 1998) may also lead to errors in the estimated GWD. For example, insufficient observations may lead to the GWD parameterization scheme used in the assimilation model dominating the resulting analysis data; the GWD inferred using ASDE could then be dominated by the assimilation model GWD parameterization. These sources of error are discussed in more detail by Pulido and Thuburn (2006). In particular, there are quantitative and qualitative differences between the GWD estimated by ASDE and the Rayleigh friction drag used in the Met Office model for that case study, which give confidence in the GWD estimation.

## 2. Model

The assimilation system for drag estimation is described in Pulido and Thuburn (2005); here we only give a concise description of the main aspects. It is

formed by three components: the dynamical model, the adjoint model, and a minimization algorithm.

The dynamical model is a three-dimensional hydrostatic primitive equation model. The predicted state variables (potential vorticity  $Q$ , horizontal divergence  $\delta$ , and density  $\sigma$ ) are represented on a hexagonal-icosahedral grid in the horizontal (Thuburn 1997) and an isentropic vertical coordinate. The horizontal resolution used in this study is  $N_c = 2562$  cells, which corresponds to a resolution of about 480 km. There are 16 vertical levels that cover from  $\sim 100$  up to 0.018 hPa. At the bottom, the Montgomery potential, taken from observations, is imposed as boundary condition. In the two uppermost layers of the model, a Rayleigh sponge layer is imposed to avoid reflection of perturbations.

The radiative transfer scheme used by the model is described in Shine (1987). It represents solar heating and the long wave effects of  $\text{CO}_2$ ,  $\text{O}_3$ , and  $\text{H}_2\text{O}$ . A zonal-mean climatology of the ozone distribution is used in the radiation calculation.

A cost function that measures the differences between observations and the model state is defined as

$$J \equiv \frac{1}{2} \sum_{l=0}^{N_l} \sum_{k=1}^{N_c} \bar{\sigma}^2 (Q_{lk} - Q_{lk}^*)^2 + (\tau \bar{\sigma})^{-2} (\sigma_{lk} - \sigma_{lk}^*)^2, \quad (1)$$

where  $Q_{lk}$  and  $\sigma_{lk}$  are model state variables at the final time  $t_f$  corresponding to the cell  $k$  and the level  $l$ ,  $Q_{lk}^*$  and  $\sigma_{lk}^*$  are observed variables that have been transformed to the model space,  $\bar{\sigma}$  is the horizontally averaged density, and  $\tau$  is a tunable time scale that has been set to a value of  $\tau = 4 \times 10^4$  s. The weights have been chosen in order to have a well-conditioned problem (see Pulido and Thuburn 2005). The height level range in (1) covers from  $\theta$  ( $p \approx 100$  hPa), which corresponds to  $l = 0$ , to  $\theta$  ( $p \approx 0.4$  hPa) (i.e., the top of Met Office analysis), which corresponds to  $l = N_l$ .

The state variables  $\mathbf{x}_f$  are given by the model evolution from  $t_0$  to  $t_f$ :

$$\mathbf{x}_f = M(\mathbf{x}_0, \mathbf{X}, t_f), \quad (2)$$

where  $\mathbf{x}_0$  is the known initial condition and  $\mathbf{X}$  are the unknown parameters, in our case the GWD. An assimilation window of 1 day is used; all observations are taken at the end of the window, and the drag  $\mathbf{X}$  is assumed independent of time during the window.

The minimization uses the conjugate gradient method to find the next minimization direction and in each direction the secant method is used. The gradient of the cost function is obtained by integrating the ad-

joint model backward over the assimilation window. The adjoint model represents the adjoint of the tangent-linear dynamic model. However, the radiation module is considered negligible in the sensitivity calculation (Pulido and Thuburn 2005).

On the first day of each month initial data  $\mathbf{x}_0$  are taken from Met Office analyses. For the rest of the month, initial data for each day are taken to be the final state of the previous day; this has the advantage that the model state evolves continuously during the month and, in particular, has no angular momentum sources due to reinitialization. However, without reinitialization there is the potential for the model state to drift over time, particularly in features that cannot be corrected by GWD such as global mean temperature at some altitude. Such drift will affect the estimated drag only indirectly, precisely because it occurs in features that are insensitive to drag. Nevertheless, after experimentation we chose one month as a suitable compromise between continuity of evolution and avoiding excessive drift.

For each day, no information about the previous day's optimum drag is used: the first guess for the minimization is set to  $\mathbf{X} = 0$ . From experiments, we conclude that 25 iterations of the conjugate gradient algorithm are enough to determine the GWD, namely, a greater number of iterations does not lead to visible changes in the GWD.

To specify the initial conditions on the first day of each month, we use Met Office analyses between 100 (the bottom of the model) and 0.4 hPa (the top of the analyses). Above this height the data are merged smoothly with data from the Committee on Space Research (COSPAR) International Reference Atmosphere climatology (Fleming et al. 1986) up to the model's highest level, about 0.018 hPa. The bottom boundary Montgomery potential on each day, and the "daily observations"  $Q_{lk}^*$  and  $\sigma_{lk}^*$  used in the cost function are also taken from Met Office analysis. We chose to analyze the year 2002 because we are confident that the Met Office analysis system was stable and did not change significantly during this year.

The top of the observational space used in (1) is 0.4 hPa. On the other hand, the control variable  $\mathbf{X}$  spans the whole model space (up to 0.018 hPa). The flow at any altitude is affected by, and so contains information on, the flow at other altitudes (e.g., Haynes et al. 1991). In principle, this nonlocal information can be extracted by the ASDE method. In practice, it is difficult to extract the information about remote altitudes because the mathematical inversion problem becomes less well conditioned (Pulido and Thuburn 2006) and, so, more

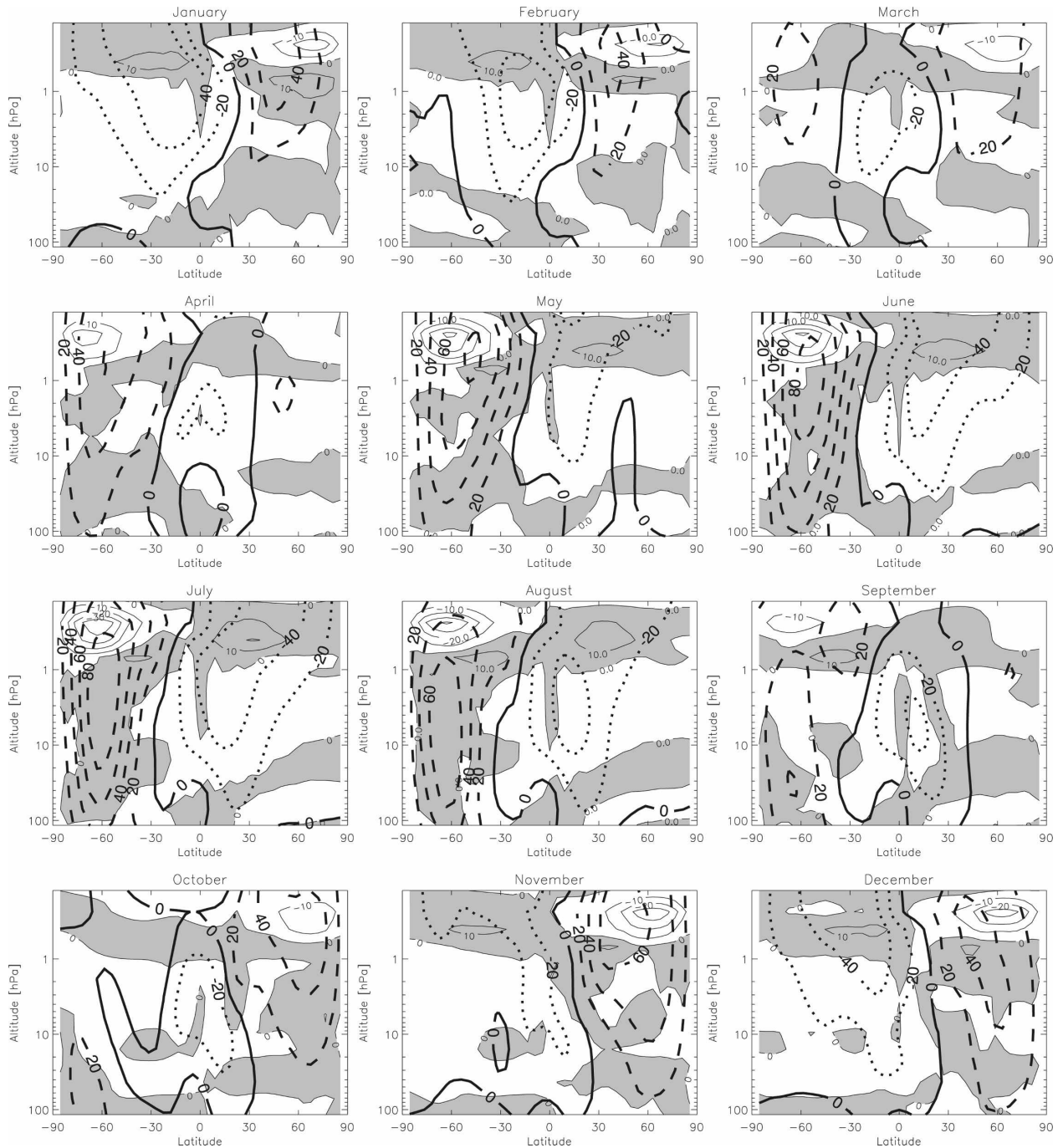


FIG. 1. Monthly averaged zonal-mean zonal component of GWD (with  $10 \text{ m s}^{-1} \text{ day}^{-1}$  contours, positive values are shaded) and the monthly averaged zonal-mean zonal wind (black contours with  $20 \text{ m s}^{-1}$ ).

susceptible to various sources of error. Thus, for altitudes above 0.4 hPa our confidence in the diagnosed GWD values quickly diminishes, so we present results only up to 0.24 hPa.

The performance of the minimization is improved by working in terms of the vertical component of curl  $\mathbf{X}$

and the horizontal divergence of  $\mathbf{X}$ , rather than directly in terms of the eastward and northward components of  $\mathbf{X}$ . However, the divergence of the flow calculated from analyses is not considered a reliable quantity. Therefore, the divergence is not used either in the initial condition on the first day of the month or as a variable

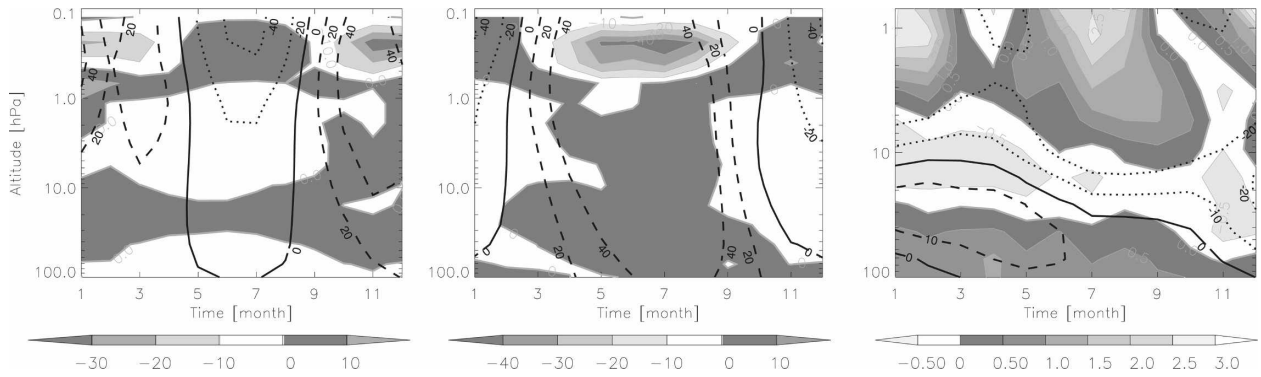


FIG. 2. Monthly averaged zonal-mean GWD (gray shading with  $10 \text{ m s}^{-1} \text{ day}^{-1}$  contours) and the monthly averaged zonal-mean wind (black contours with  $20 \text{ m s}^{-1}$ ) at (left)  $60^\circ\text{N}$ , (middle)  $-60^\circ\text{S}$ , and (right) on the equator. The right-hand panel extends up to 2 hPa to focus on the lower midstratosphere since GWD is much greater aloft.

in the cost function. Consequently, divergent drag, even when we keep it in the control space, is not constrained by divergence observations, so we do not expect it to be realistic (Pulido and Thuburn 2006). In this work we therefore focus on the rotational drag (converted back to zonal and northward components for clarity of presentation); some discussion of the divergent drag is given in the appendix.

### 3. Results

#### a. Zonal-mean zonal drag

Figure 1 presents the monthly mean zonally averaged GWD for the year 2002. The most prominent pattern is the winter deceleration center, which reaches values of  $-49 \text{ m s}^{-1} \text{ day}^{-1}$  in July and is centered at a latitude of  $63^\circ\text{S}$ . During boreal winter maximum decelerations are about  $-38 \text{ m s}^{-1} \text{ day}^{-1}$  in November. The deceleration center is located poleward of the winter jet, particularly during boreal winter. Peak amplitudes are at a height of 0.24 hPa; however, we cannot draw a definitive conclusion about the height of peak amplitudes since they are located at the top of the observational space.

Although the winter stratospheric jet in the Southern Hemisphere in June presents important differences from that in the Northern Hemisphere in December, in strength and also in geometry (Fig. 1), the estimated winter deceleration centers are remarkably similar in the height–latitude distribution except for a strength factor. The winter deceleration centers in both hemispheres are found at latitude  $\sim 63^\circ\text{S}$ , altitude 0.24 hPa, despite significant interhemispheric differences and seasonal evolution in the structure of the winter jets. Closer inspection shows some day-to-day variability (Fig. 3) and some longitudinal structure (Fig. 14) in the

latitude of maximum drag. The fixed altitude of the maximum drag might be partly explained by the coarse vertical resolution used near the top of the ASDE model.

In summer, there is also a deceleration center located at lower latitudes,  $\sim 30^\circ$ . Maximum amplitudes reach  $20 \text{ m s}^{-1} \text{ day}^{-1}$ . The deceleration center is located at a slightly lower height  $\sim 0.6$  hPa. This behavior is not coherent with a Lindzen (1981) picture of gravity wave breaking in which a much higher deceleration center is expected in summer. The explanation for this is that the summer jet is not completely represented in our model; maximum wind speed is located near the top of observations so that the summer GWD deceleration center, which is expected above the jet, is not being captured by ASDE. Using CIRA data, Marks (1989) found a weak summer deceleration center at about 0.1 hPa and some evidence of a much stronger deceleration center above 0.01 hPa.

At lower heights, say 10–1 hPa, the GWD tends to accelerate both the eastward winter jet and westward summer jet. This results in a dipolar pattern, with deceleration above the jet core and acceleration below. Drag values in the winter acceleration center exceed  $10 \text{ m s}^{-1} \text{ day}^{-1}$ , though the acceleration tendency extends downward throughout most of the winter stratosphere. The dipolar pattern appears most marked in the northern winter (e.g., in January). In southern winter (e.g., in August) the acceleration center is offset toward lower latitudes. These differences between hemispheres in the details of the drag appear to be related to differences in the details of the jet structure. The acceleration below the jet core is consistent with the idea of gravity wave filtering; waves with phase speeds in the same direction as the jet are filtered below the jet core, accelerating the jet. A similar pattern of acceleration of

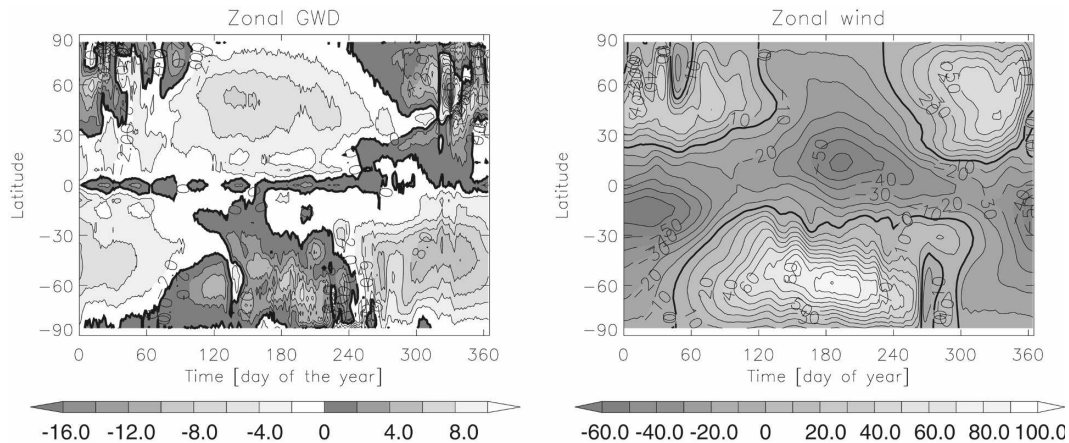


FIG. 3. (left) Zonal-mean GWD as a function of latitude and time at 0.24 hPa. A 10-day window averaging is used. The contour interval is  $5 \text{ m s}^{-1} \text{ day}^{-1}$  (note resetting of grayscale). (right) Zonal-mean zonal wind at 0.24 hPa. The contour interval is  $10 \text{ m s}^{-1}$ .

the winter jets by GWD has also been inferred from zonal-mean budget studies (Marks 1989; Alexander and Rosenlof 1996).

At the lowest heights, 100–10 hPa, the GWD is weaker  $\leq 8 \text{ m s}^{-1} \text{ day}^{-1}$ . As noted already, the winter hemisphere GWD is predominantly eastward, tending to accelerate the winter eastward jet. The southern summer GWD is predominantly westward, though not uniformly so. The northern summer GWD shows a striking band of eastward GWD, extending from the equator near 100 hPa to the North Pole near 10 hPa, against a background of westward GWD, which persists from May to September. We currently have no explanation for this feature.

In March–April and September–October the GWD

exhibits smooth transitions synchronized with zonal wind changes. In September the winter deceleration center is particularly weak. This behavior can be traced back to the early breaking of the Antarctic vortex through the unprecedented sudden stratospheric warming that took place in 2002. In normal years we expect a longer-lived winter deceleration center that must persist in September and start weakening in October, as found by Marks (1989).

In the height range 10–1 hPa within about  $5^{\circ}$ – $10^{\circ}$  of the equator the GWD appears to evolve independently of higher latitudes (see Fig. 1). This behavior is likely to be related to the SAO in zonal wind at those heights. At both lower and higher altitudes the equatorial GWD does appear to be well correlated with that at higher

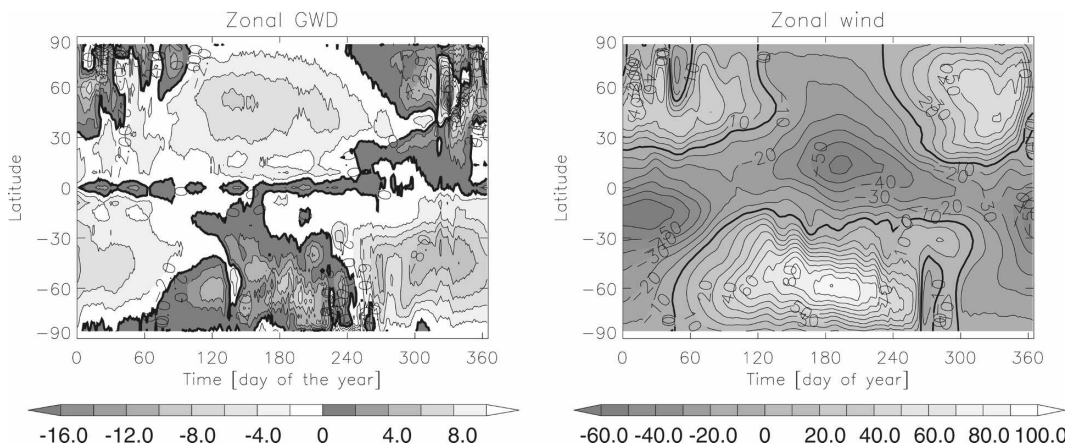


FIG. 4. (left) Zonal-mean GWD as a function of latitude and time at 1.15 hPa. To diminish noise a 10-day window averaging was used. The contour interval is  $2 \text{ m s}^{-1} \text{ day}^{-1}$  (note resetting of grayscale). (right) Zonal-mean zonal wind at 1.15 hPa. The contour interval is  $10 \text{ m s}^{-1}$ .

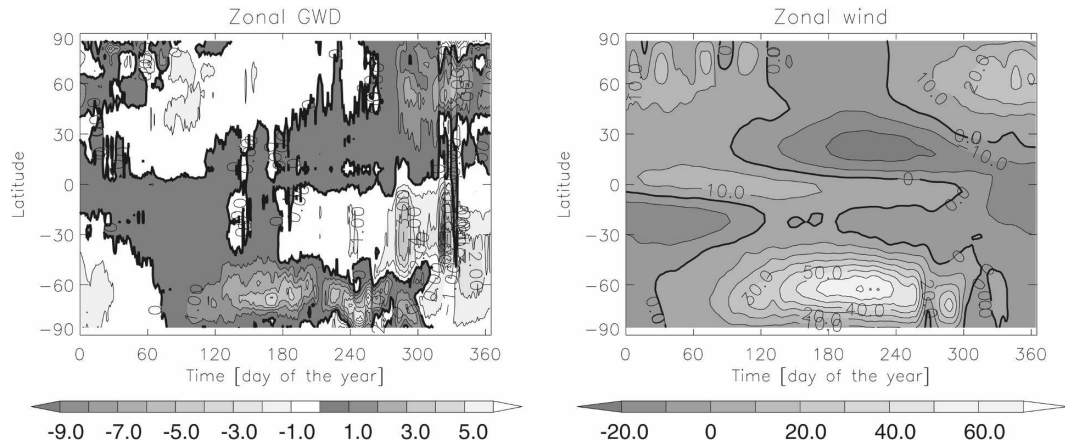


FIG. 5. (left) Zonal-mean GWD as a function of latitude and time at 40 hPa. To diminish noise a 10-day window averaging was used. The contour interval is  $1 \text{ m s}^{-1} \text{ day}^{-1}$  (note resetting of grayscale). (right) Zonal-mean zonal wind at 40 hPa. The contour interval is  $10 \text{ m s}^{-1}$ .

latitudes. The equatorial GWD behavior is discussed in detail later.

#### b. GWD seasonal variability

Figure 2 presents the monthly averaged zonal-mean GWD at three different latitudes:  $60^\circ\text{N}$ ,  $60^\circ\text{S}$ , and at the equator. The patterns show similarities between the Northern and Southern Hemisphere (left and middle panels), such as the winter deceleration center at 0.24 hPa with eastward acceleration below and the summer deceleration above 1 hPa, with westward acceleration below. The dipolar structure at the end of boreal winter (left panel) is not found at austral winter. At lower heights, below 10 hPa, there is some asymmetry between the GWD in the two hemispheres, particularly in the summer.

The right panel of Fig. 2 shows the evolution of the monthly averaged zonal wind (contours) and zonal-mean GWD (gray shading) at the equator. In this year, the westward phase of the QBO descends from about 10 hPa in January to about 100 hPa in December. The

estimated GWD shows a westward forcing region that descends together with the zero zonal wind line. GWD values are about  $-0.5 \text{ m s}^{-1} \text{ day}^{-1}$ . Similar tendencies have been found by Alexander and Rosenlof (2003) using a zonal-mean budget study in a 6-yr period. Their estimated values appear to be slightly smaller, around  $-0.25 \text{ m s}^{-1} \text{ day}^{-1}$ . The SAO pattern is also captured by ASDE: GWD above  $\sim 5$  hPa shows a semiannual cycle with peak eastward forcing of about  $2.5 \text{ m s}^{-1} \text{ day}^{-1}$  and a weaker westward forcing of about  $-0.5 \text{ m s}^{-1} \text{ day}^{-1}$ .

Next we examine the GWD seasonal cycle as a function of latitude. At 0.24 hPa, GWD shows an annual oscillation in extratropical regions (Fig. 3) with maximum westward GWD during winter and maximum eastward GWD in summer, as expected. The winter deceleration centers in both hemispheres show significant short time scale variability; a 10-day window averaging has been applied to make the contour plots clearer—Fig. 6 shows a sample of unfiltered data. The summer deceleration centers, on the other hand, show

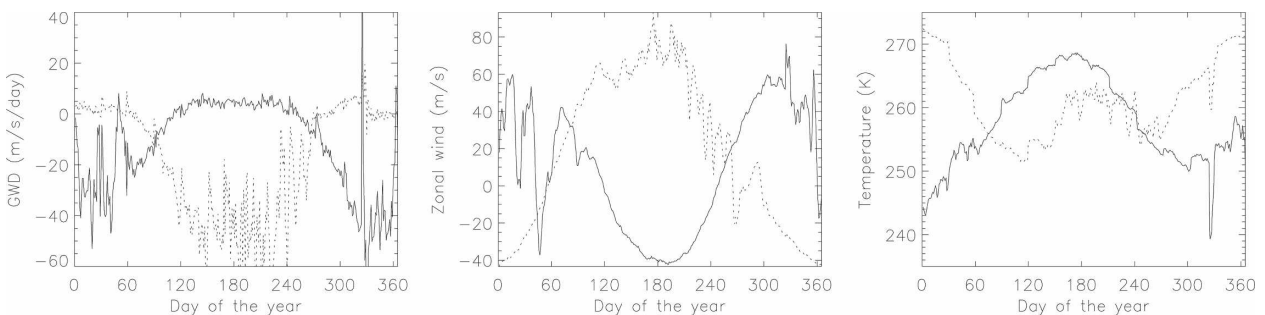


FIG. 6. Daily evolution of the (left) zonal-mean GWD, (middle) zonal wind, and (right) temperature at 0.24 hPa. The latitude is  $60^\circ\text{N}$  (continuous line) and  $60^\circ\text{S}$  (dotted line).

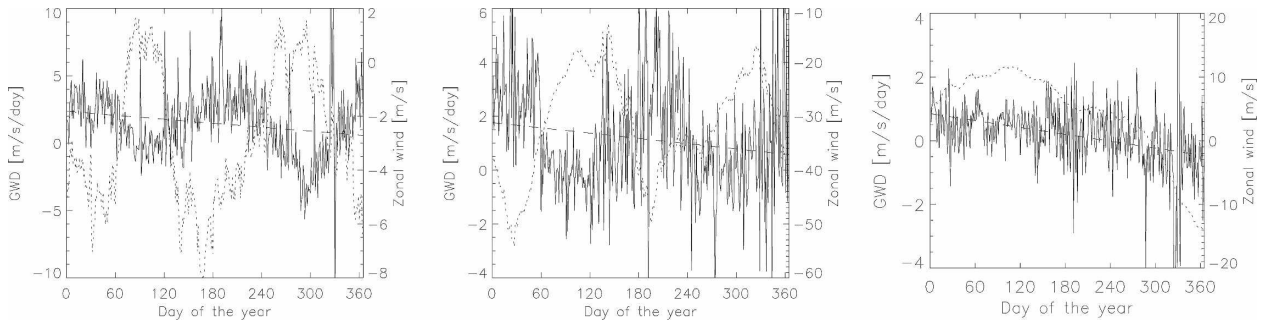


FIG. 7. Daily evolution of the zonal-mean GWD (continuous line), zonal wind (dotted line) on the equator at (left) 0.24 hPa, (middle) 1.15 hPa, and (right) 40 hPa.

much less short time scale variability. It is likely that these winter – summer differences in drag variability are related to winter – summer differences in zonal wind variability (right panel of Fig. 3) and in Rossby wave activity. GWD also appears to be sensitive to the stratospheric sudden warmings that occurred in both hemispheres in 2002, (e.g., around day 25 and 55 in the Northern Hemisphere and around day 265 in the Southern Hemisphere). The estimated GWD itself does not reverse sign at this altitude, though it does at 0.40 hPa (not shown). The anomalous feature in the zonal drag on day 325 will be discussed further in the next section. As already noted, maximum magnitudes in GWD in the winter hemisphere are located poleward of the winter jet, while maximum GWD values in the summer hemispheres are located equatorward of the summer jet.

At 1.15 hPa, the zonal GWD has predominantly the same sign as the zonal wind (Fig. 4). The GWD exhibits high variability, particularly in the winter hemisphere. Typical magnitudes are much weaker than at 0.24 hPa, with peaks of  $10 \text{ m s}^{-1} \text{ day}^{-1}$  in the winter hemisphere

and  $4 \text{ m s}^{-1} \text{ day}^{-1}$  in the summer hemisphere. In the summer hemisphere westward GWD appears to maximize during the build-up of the summer jet. At the equator, there are latitudinally concentrated eastward GWD centers. If they are believable (their scale is close to the grid scale used in the ASDE model, though they are consistent with the forcing required to drive the SAO), then it is likely that they are due to equatorially trapped waves such as Kelvin waves.

GWD at lower altitudes is quite noisy (Fig. 5). However the sign of the GWD is predominantly such as to accelerate the prevailing zonal jets. On the equator as the zonal wind changes from eastward to westward, related to the descending QBO zero wind line shown in the right panel of Fig. 2, the zonal drag also changes from eastward to westward. As already mentioned, the estimated forcing is in accord with that required to drive the QBO.

### c. GWD day-to-day variability

The assimilation technique is able to estimate GWD with a temporal resolution of the order of a day, which

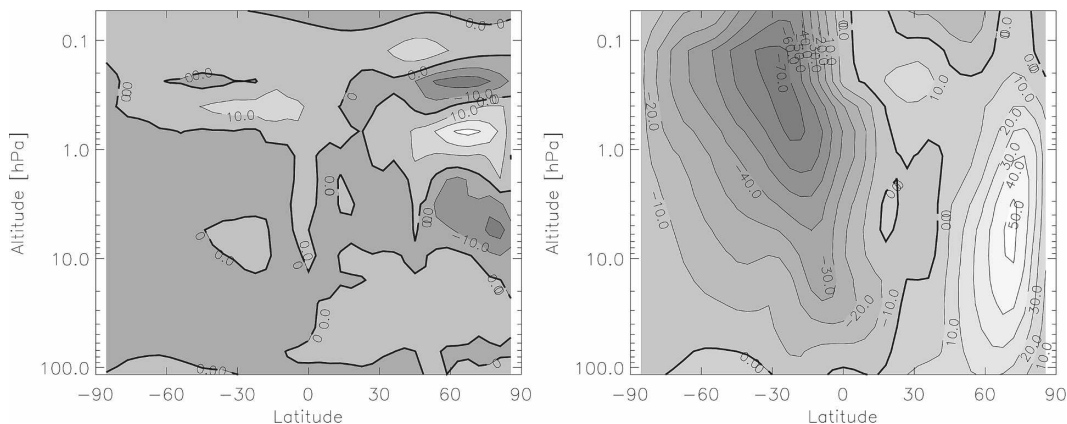


FIG. 8. (left) Zonal-mean GWD and (right) zonal-mean zonal wind on 26 Dec 2002. The contour intervals are  $10 \text{ m s}^{-1} \text{ day}^{-1}$  and  $10 \text{ m s}^{-1}$ , respectively.

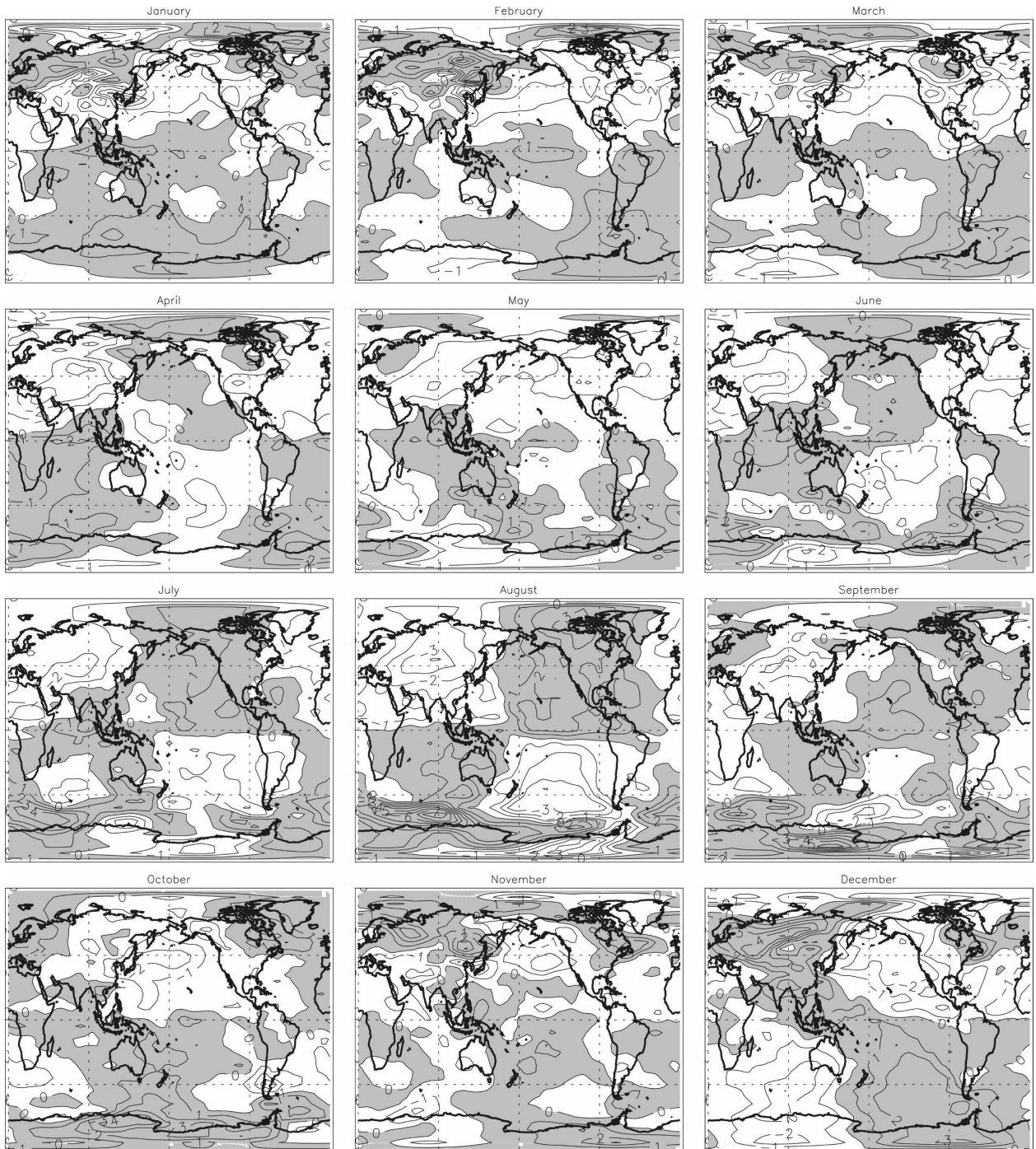


FIG. 9. Monthly averaged mass-weighted height integral of the zonal GWD (contour interval is  $0.01 \text{ N m}^{-2}$ , label units are in  $0.01 \text{ N m}^{-2}$ ). Positive values are shaded.

is the temporal resolution of the employed Met Office analysis. This enables us to study the day-to-day variability of GWD.

The daily evolution of zonal-mean GWD at  $60^\circ\text{N}$  and  $60^\circ\text{S}$  (Fig. 6) shows a relatively smooth evolution during summer but large-amplitude day-to-day variability in

winter. This feature is visible in both hemispheres and is correlated with the mean zonal flow, which is also highly variable in winter (middle panel of Fig. 6). In general, variations in the GWD are quite well anticorrelated with variations in the zonal wind. For example, in the Northern Hemisphere the eastward zonal wind

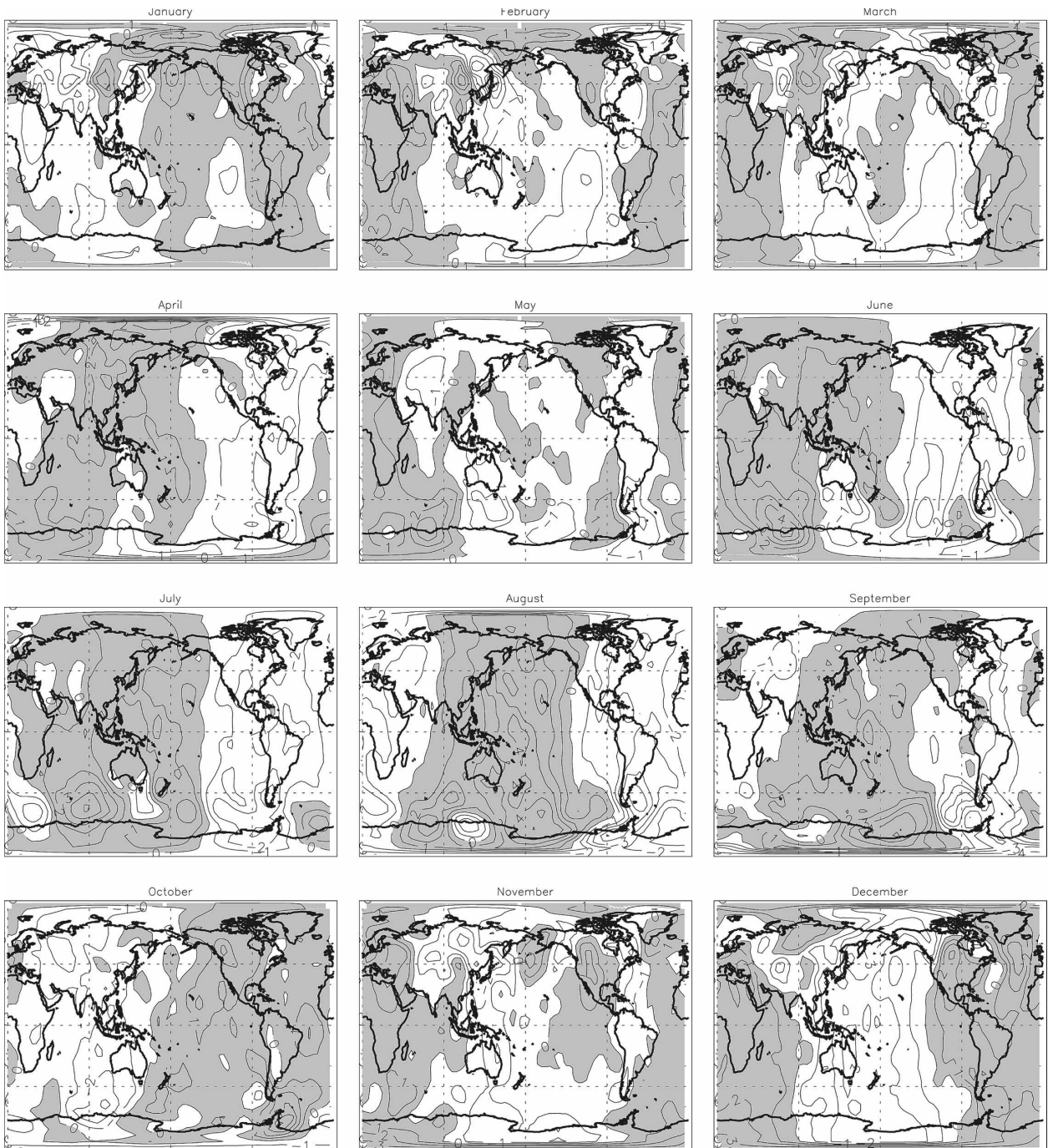


FIG. 10. As in Fig. 9 but of the meridional GWD.

decelerates sharply around day 25 and again around day 55, accompanied by sharp reductions in the westward GWD. In the Southern Hemisphere the zonal wind reverses from eastward to westward around day 265 during the unusual sudden warming, and at the same time the zonal GWD changes sign.

An anomalous peak is found in zonal GWD on day

325, that is, 21 November (left panel of Fig. 6). This peak coincides with a sharp drop in temperature of about 10 K in both hemispheres and a corresponding jump in the Northern Hemisphere jet strength. This unphysical behavior suggests a problem with the analysis data for that day.

On the equator, at 0.24 and 1 hPa the daily GWD

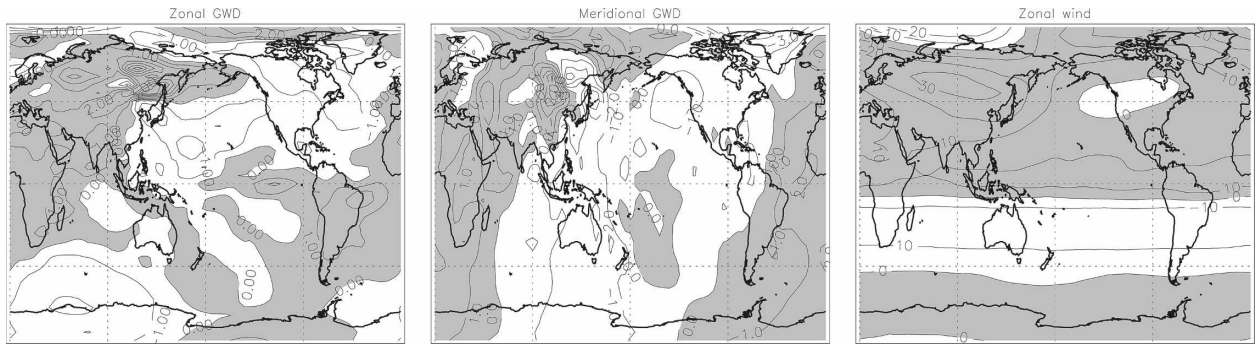


FIG. 11. Monthly averaged GWD at 40 hPa in February: (left) zonal and (middle) meridional component ( $1 \text{ m s}^{-1} \text{ day}^{-1}$ ). (right) Monthly averaged zonal wind at 40 hPa ( $10 \text{ m s}^{-1}$ ).

shows considerable day-to-day variability superposed on a clear semiannual oscillation with an amplitude of about  $5 \text{ m s}^{-1} \text{ day}^{-1}$  (left and middle panels in Fig. 7). At 40 hPa (right panel in Fig. 7) again there is considerable day-to-day variability, now superposed on a systematic negative trend of  $-1.31 \text{ (m s}^{-1} \text{ day}^{-1}) \text{ yr}^{-1}$ , which correlates with the QBO variation in zonal wind. There is also a negative trend at higher altitudes in addition to the semiannual oscillation. The trend is  $-1.79 \text{ (m s}^{-1} \text{ day}^{-1}) \text{ yr}^{-1}$  at 0.24 hPa and  $-1.19 \text{ (m s}^{-1} \text{ day}^{-1}) \text{ yr}^{-1}$  at 1.15 hPa. With only one-year assimilation we are not able to assess the causes of these high altitude trends and whether they are related to the QBO.

On 28 December 2002 a strong increasing of GWD is found that reaches positive values, at  $60^\circ\text{N}$  and 0.24 hPa (Fig. 6). The GWD estimated for a previous day, 26 December 2002, is shown in Fig. 8 in order to examine how the transition occurs and its relation to the zonal-mean zonal wind. A tripolar structure is found at northern high latitudes, with eastward GWD at 0.7 hPa and westward GWD both above and below. The highest deceleration center remains at 0.24 hPa, even when the jet core is located much lower (Fig. 8, right panel). As the season evolves the westward GWD center at 0.24 hPa weakens until it disappears, while the eastward GWD center gets stronger. This could be evidence of gravity wave source variability since the filtering mechanism of a constant isotropic gravity wave spectrum cannot explain directly this behavior.

#### d. Horizontal GWD dependencies

The upward flux of zonal pseudomomentum at the bottom of the model, assuming the horizontal divergence of fluxes and fluxes at the top are negligible, is given by

$$F_b = \int_{\theta_b}^{\theta_t} \sigma X_x d\theta. \quad (3)$$

An analogous expression holds for the upward flux of northward pseudomomentum. Thus, in principle, we can obtain information on gravity wave sources from vertical profiles of GWD. For this calculation we take  $\theta_t = \theta(p = 0.24 \text{ hPa})$ . Because the density  $\sigma$  decreases rapidly with altitude, the integral is dominated by the lower and middle stratosphere, and the results are insensitive to the exact location of the top boundary and the neglect of top boundary fluxes. Drag values greater than about  $1000 \text{ m s}^{-1} \text{ day}^{-1}$  would be needed above  $\theta_t$  in order to make a significant difference to the column integrals; such values are beyond the extreme values predicted by current typical GWD schemes (e.g., McLandress and Scinocca 2005).

The monthly mean estimated upward fluxes are shown in Figs. 9 and 10. Both components show the greatest signals over land in the winter hemisphere. The largest zonal component is  $0.09 \text{ N m}^{-2}$  in August at  $-58.5^\circ$  latitude,  $85.5^\circ$  longitude. Positive and negative values tend to occur together forming dipoles, which tend to be aligned north-south in the zonal component and east-west in the meridional component. Confidence in these results is limited because the vertical integrals are dominated by the lowest altitudes in the model domain where the estimated drag appears noisy. Several different mechanisms have been hypothesized as potential tropospheric sources for gravity waves that propagate into the middle atmosphere, including orography, convection, and spontaneous emission, but these sources have not been reliably quantified globally. Our results suggest some correlation with regions of large orography, but are not clear enough to add much to this debate.

The monthly mean GWD at 40 hPa is strongly correlated with the monthly mean vertically integrated GWD; this is as expected because the mass weighting means that the vertical integral is dominated by the lower stratosphere. We show the most active months in each hemisphere, February and August, in Figs. 11 and

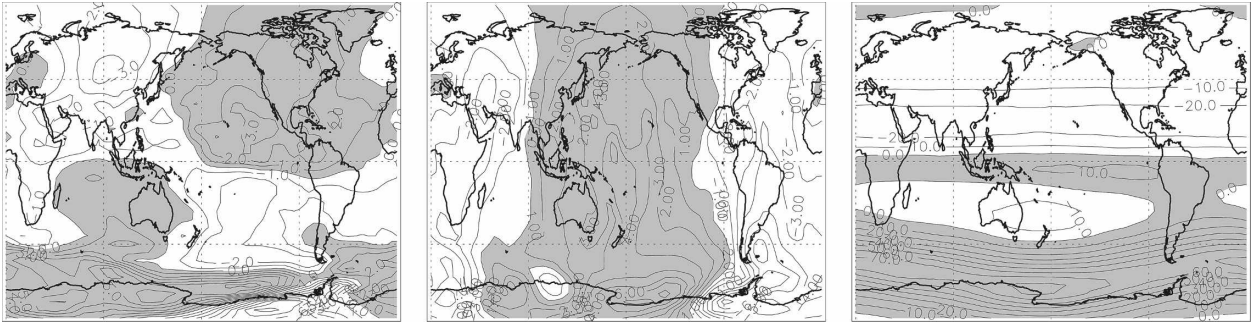


FIG. 12. As in Fig. 11 but in August.

12, respectively. GWD maximizes in the exit region of the jet streaks in both hemispheres (right panels of Figs. 11 and 12).

At 1.15 hPa, eastward zonal forcing (Fig. 13) is found concentrated on the equator during January–February and July–August. The sign and latitudinal scale of this drag is consistent with forcing by Kelvin waves with a vertical wavelength of 2–3 km; however, the features are close to our horizontal resolution limits (in ASDE and in the Met Office analysis). Peak values appear to be over the oceans. As expected there is no sign of this feature in the meridional drag (not shown).

At 0.24 hPa, GWD shows a strong, but not perfect, anticorrelation with large-scale flow features in both the zonal and meridional components (Fig. 14). In the Southern Hemisphere winter meridional GWD is dominated by a wave 1 pattern. This GWD pattern and the meridional wind appear to be in quadrature in July. On the other hand, they appear to be in antiphase in August. In the Northern Hemisphere in November, the meridional GWD and wind components are approximately in quadrature. The GWD at 0.24 hPa also shows wavelike patterns in the summer hemisphere. The me-

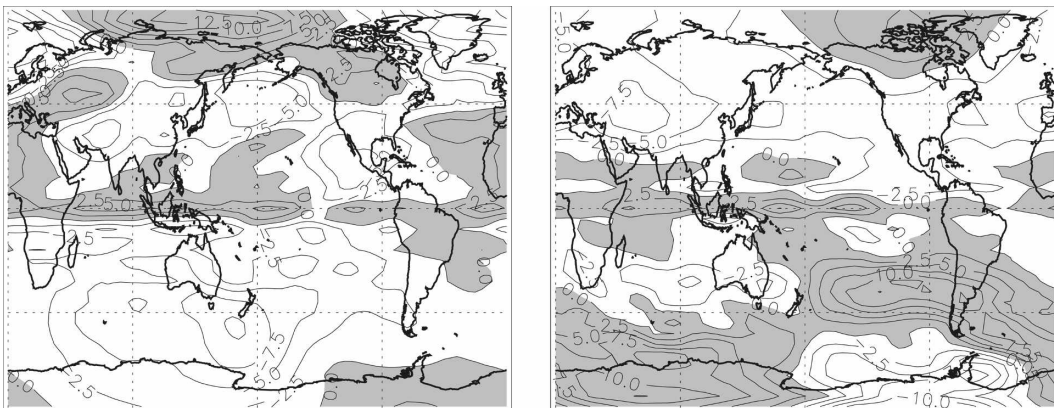
ridional component shows wave 2 or wave 3 patterns with maximum amplitudes of  $7.5 \text{ m s}^{-1} \text{ day}^{-1}$  at mid-latitudes.

As found at 40 hPa, the zonal GWD peaks at the exit region of the jet streaks. GWD deceleration centers are located, in general, poleward or eastward of the jet streaks. This is particularly visible at  $60^\circ\text{S}$  in July (Fig. 14).

#### 4. Conclusions

We have applied an assimilation technique to estimate gravity wave drag for a whole year of observations. The seasonal cycle of estimated zonal-mean zonal drag shows reasonable patterns and strength. They are consistent with previous estimates using budget studies. Also, they are broadly consistent with gravity wave filtering ideas, though careful inspection shows exceptions, for example, the tripole pattern in Fig. 8; reproducing such patterns would be a challenge for current GWD parameterization schemes.

The assimilation technique estimates a zonal-mean deceleration center just above the winter jet core and acceleration below, broadly in agreement with filtering

FIG. 13. Monthly averaged zonal component of GWD at 1.15 hPa (left) in February and (right) in August (contour interval is  $2.5 \text{ m s}^{-1} \text{ day}^{-1}$ ).

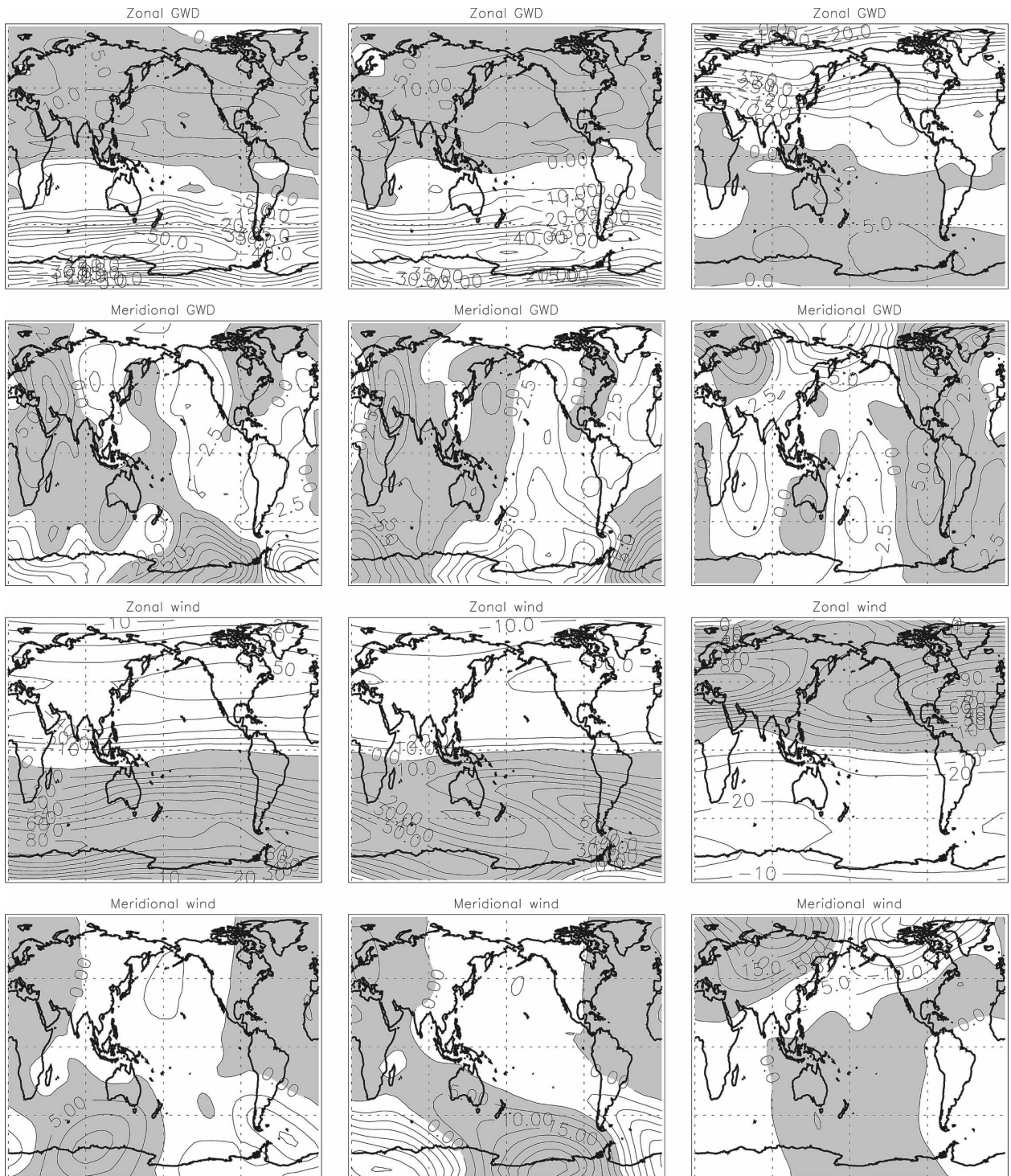


FIG. 14. Monthly averaged fields at 0.24 hPa in (left) July, (middle) August, and (right) November. (from top to bottom) The fields are zonal and meridional GWD component ( $\text{m s}^{-1} \text{day}^{-1}$ ) and zonal and meridional wind component ( $\text{m s}^{-1}$ ).

mechanism predictions. These features have also been found with zonal-mean budget studies (Alexander and Rosenlof 1996). The summer hemisphere also has a zonal-mean deceleration center above the jet core and

acceleration below. A dipole pattern is present in the winter–spring transition. The dipolar pattern is stronger in the Northern Hemisphere than in the Southern Hemisphere (see Figs. 1 and 2). The positive accelera-

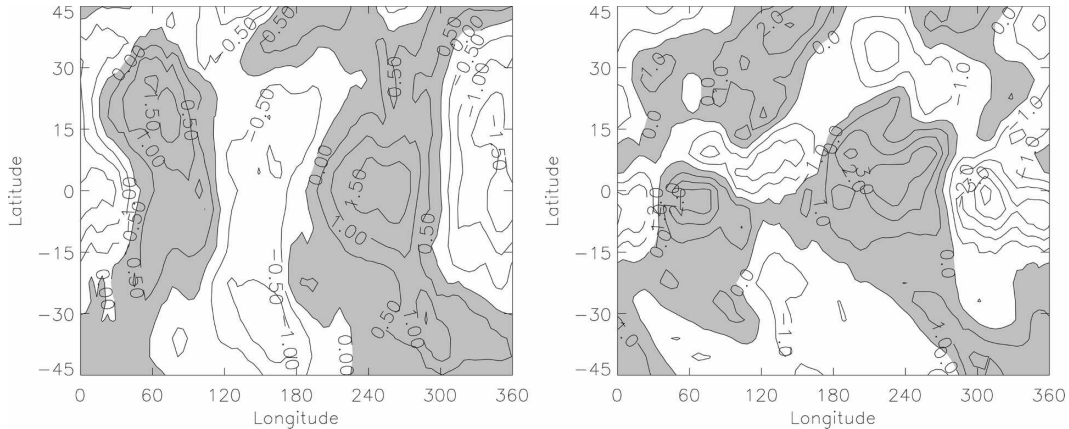


FIG. A1. Monthly averaged (left) temperature (contour interval 0.5 K) and (right) zonal wind (contour interval  $1 \text{ m s}^{-1}$ ) differences at the model bottom layer between the control model evolution and Met Office analyses in March.

tion center located below the winter deceleration center is strongest in January–February in the Northern Hemisphere. This behavior may be related to the structure of the winter stratospheric jet, which is more tilted and located in lower latitudes in the Northern Hemisphere.

The location of the winter zonal-mean deceleration center does not vary. In both northern and southern winters, its center is at  $63^\circ$  and 0.24 hPa. Regrettably, the top of the observational space is at 0.4 hPa. Although the GWD components are estimated up to the model top (about 0.018 hPa) the lack of observations may influence the height of the GWD center, especially in the summer where a higher deceleration center is expected. The Southern Hemisphere was particularly perturbed in 2002 so that Southern Hemisphere GWD patterns were probably more similar than usual to those in the Northern Hemisphere. In normal years we expect stronger interhemispheric differences, as discussed by Shine (1989).

Although the winter deceleration centers in the two hemispheres are similar in magnitude and height, their maximum strength is attained in different seasons (Fig. 1). In the Northern Hemisphere, the winter deceleration center maximizes in late autumn (November), while in the Southern Hemisphere it maximizes in winter (July).

The longitudinal structure of GWD appears to be related to the wind patterns. However, their correlation is not unique. In the Southern Hemisphere lower mesosphere we found that the large-scale wave patterns of meridional GWD and meridional wind are in antiphase during August, while they are in quadrature during July in the Southern Hemisphere and during February in the Northern Hemisphere (Fig. 14).

The GWD is expected to be small near the equator compared with high latitude drag. Moreover, the errors in drag estimation technique are expected to be largest there (Pulido and Thuburn 2005). However, the results for low latitudes appear realistic and are comparable with those obtained by other techniques. The estimated GWD in low latitudes shows that westward forcing descends together with the westward QBO phase. At higher altitudes GWD shows a semiannual pattern that is approximately out of phase with the SAO wind.

One outcome of this work is that we now have a database of daily three-dimensional drag fields to accompany the Met Office wind and temperature analyses for the year 2002. We plan to use this database to estimate optimal parameters for one or more GWD parameterization schemes. Another follow-up study is an examination of the interannual variability of GWD, however GWD estimations may be affected by the changes introduced in the Met Office assimilation system (among others, the implementation of a three-dimensional variational assimilation system in 2000 and of a gravity wave parameterization in 2003) so that the GWD sensitivity to these changes needs to be addressed.

## APPENDIX

### Wave 2 Pattern in the Divergent GWD

For the reasons discussed in section 2, we have not shown results for the divergent component of GWD in the main body of this paper. The divergent GWD estimated by ASDE gives a global-scale wave 2 pattern, which is particularly visible in the height-integrated divergent GWD. The wave pattern maximizes in March and September.

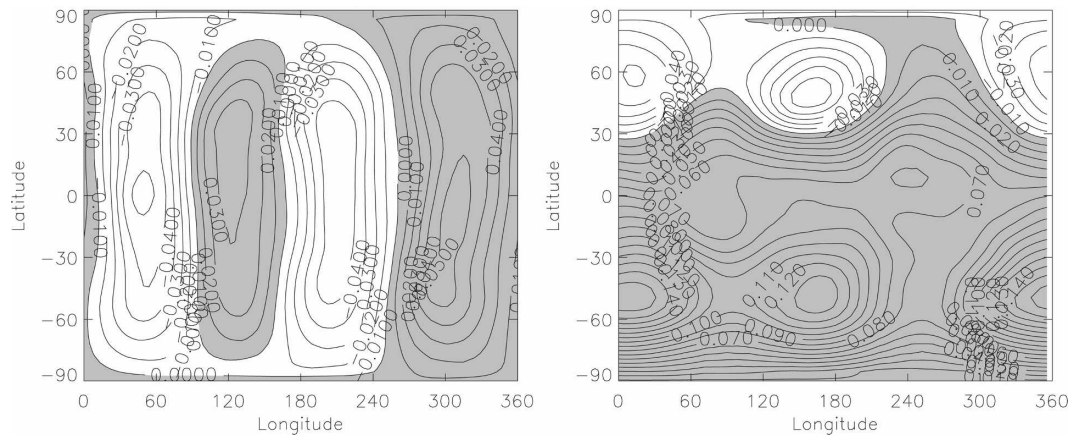


FIG. A2. Monthly averaged (left) zonal and (right) meridional components of the divergent GWD integrated in height for the estimation in March (contour interval  $0.01 \text{ N m}^{-2}$ ).

Figure A1 shows the temperature and zonal wind differences between the model without drag (i.e., without divergence and rotational drag components) and analysis at the lowest model layer for March 2002 when differences are largest. There is a persistent wave 2 pattern within the tropics. The estimated GWD contains a wave 2 pattern in the divergent drag that is present in zonal and meridional components (Fig. A2). This GWD is such as to reduce the bias between the model and analyses.

The cause of this artificial wave 2 pattern is a bad representation of the semidiurnal tide and can be traced back to two problems related to ASDE. One is the bottom boundary Montgomery potential, which is prescribed from Met Office analyses and therefore has a one-day resolution, so the bottom boundary tidal signal always has the same phase, that is, it is aliased into the time mean. The second is that the semidiurnal tide generated internally in the ASDE model by radiative forcing has larger amplitude at the stratopause than the semidiurnal tide in the Met Office analyses. In fact, the analyses are known to underestimate the tides, so we expect that the real tidal amplitude is somewhere between that of the analyses and that of the ASDE model.

A deeper examination of this problem is not possible since Met Office analyses only have a one-day resolution and, therefore, do not represent the evolution of tides. We performed experiments where a selective wave 2 filter was applied to the bottom boundary data so that the problem was reduced, but the application of the filtering technique adds arbitrariness, and the results were not conclusive. Since the limitation is in the temporal resolution of the analysis data rather than in the technique, we have kept the application of the assimilation technique as transparent as possible.

The relevant information for the general circulation is in the rotational drag since this is the component that may produce long-term effects, as discussed in Pulido and Thuburn (2005). On the other hand, divergent drag produces a transitory response in the flow with no long-term effects. Moreover, the divergent drag is more severely affected than the rotational drag by model and data errors. Because of this, we focus on the analysis in the rotational drag, which is free of the problems related to the bad representation of tides.

#### REFERENCES

- Alexander, M. J., and K. H. Rosenlof, 1996: Nonstationary gravity wave forcing of the stratospheric zonal mean wind. *J. Geophys. Res.*, **101**, 23 465–23 474.
- , and —, 2003: Gravity-wave forcing in the stratosphere: Observational constraints from the Upper Atmosphere Research Satellite and implications for parameterization in global models. *J. Geophys. Res.*, **108**, 4597, doi:10.1029/2003JD003373.
- Bowman, K. P., K. Hoppel, and R. Swinbank, 1998: Stationary anomalies in stratospheric meteorological data sets. *Geophys. Res. Lett.*, **25**, 2429–2432.
- Fleming, E. L., S. Chandra, J. J. Barnett, and M. Corney, 1986: Zonal mean temperature, pressure, zonal wind and geopotential height as functions of latitude. *Adv. Space Res.*, **10**, 11–59.
- Hamilton, K., 1983: Diagnostic study of the momentum balance in the Northern Hemisphere winter stratosphere. *Mon. Wea. Rev.*, **111**, 1434–1441.
- Haynes, P. H., C. J. Marks, M. E. McIntyre, T. G. Shepherd, and K. P. Shine, 1991: On the downward control of extratropical diabatic circulations by eddy-induced mean zonal forces. *J. Atmos. Sci.*, **48**, 651–678.
- Hines, C. O., 1997: Doppler spread parametrization of gravity-wave momentum deposition in the middle atmosphere. Part 1: Basic formulation. *J. Atmos. Sol. Terr. Phys.*, **59**, 371–386.
- Lindzen, R. S., 1981: Turbulence and stress owing to gravity wave and tidal breakdown. *J. Geophys. Res.*, **86**, 9707–9714.
- Marks, C. J., 1989: Some features of the climatology of the middle

- atmosphere revealed by *Nimbus 5* and *6*. *J. Atmos. Sci.*, **46**, 2485–2508.
- McLandress, C., and J. F. Scinocca, 2005: The GCM response to current parameterizations of nonorographic gravity wave drag. *J. Atmos. Sci.*, **62**, 2394–2413.
- Murgatroyd, R. J., and F. Singleton, 1961: Possible meridional circulations in the stratosphere and mesosphere. *Quart. J. Roy. Meteor. Soc.*, **87**, 125–135.
- Pulido, M., and J. Thuburn, 2005: Gravity wave drag estimation from global analyses using variational data assimilation principles. I: Theory and implementation. *Quart. J. Roy. Meteor. Soc.*, **131**, 1821–1840.
- , and —, 2006: Gravity wave drag estimation from global analyses using variational data assimilation principles. II: A case study. *Quart. J. Roy. Meteor. Soc.*, **132**, 1527–1543, doi:10.1256/qj.05.43.
- Shine, K., 1987: The middle atmosphere in the absence of dynamical heat fluxes. *Quart. J. Roy. Meteor. Soc.*, **113**, 603–633.
- , 1989: Sources and sinks of zonal momentum in the middle atmosphere diagnosed using the diabatic circulation. *Quart. J. Roy. Meteor. Soc.*, **115**, 265–292.
- Swinbank, R., and A. O'Neill, 1994: A stratosphere troposphere data assimilation system. *Mon. Wea. Rev.*, **122**, 686–702.
- Thuburn, T., 1997: A PV-based shallow-water model on a hexagonal-icosahedral grid. *Mon. Wea. Rev.*, **125**, 2328–2347.
- Warner, C. D., and M. E. McIntyre, 1996: On the propagation and dissipation of gravity wave spectra through a realistic middle atmosphere. *J. Atmos. Sci.*, **53**, 3213–3235.